J. Fluid Mech. (1985), *vol.* 158, *pp.* 47–70
Printed in Great Britain

Shoaling gravity waves: comparisons between field observations, linear theory, and a nonlinear model

By STEVE ELGAR AND R. T. GUZA
Scripps Institution of Oceanography, A-022, University of California, La Jolla, California 92093

(Received 29 November 1984)

Observed statistics of non-breaking ocean-surface gravity waves shoaling between 4 and 1 m depths are compared with the predictions of linear finite-depth theory and a nonlinear model. The linear theory included effects of the directional distribution of energy within each frequency component. The nonlinear model, which does not consider directional effects, is based on Boussinesq-type equations for a sloping bottom (Freilich & Guza 1984). Given initial conditions in 4 m depth, the nonlinear model more accurately predicts the evolution of energy spectra, coherence and phase speed between sensors, and lengths of runs of high waves than does the linear theory. In four out of five cases, observed trends in the evolution of sea-surface-elevation skewness are predicted by the nonlinear model, while linear theory predicts zero skewness. Neither model can explain changes in the directional spectra observed between 9 and 4 m depths.

1. Introduction

As ocean surface gravity waves shoal the wave field can undergo substantial nonlinear evolution from its deep-water state. Narrowband spectra develop secondary peaks at harmonics of the peak frequency, while broadband spectra often show an increase in energy over a wide range of frequencies higher than the most energetic part of the spectrum. Along with this amplitude evolution, phases of the various frequency components also evolve, sometimes resulting in phase velocities substantially different from those predicted by the linear finite-depth dispersion relationship (Inman, Tait & Nordstrom 1971; Büsching 1978; Thornton & Guza 1982; and others). The shape of individual shoaling waves also changes, from an almost symmetrical profile in deep water to a shape with sharp crests and broad, flat troughs in shallow water. This change in wave shape is partially reflected by the evolution of sea-surface-elevation skewness. The mean lengths of runs of high waves also show significant evolution as the wave field shoals (Elgar, Guza & Seymour 1984).

Linear finite-depth theory (LFDT) does not predict the transformation of many of the statistics of a shoaling wave field. On the other hand, the nonlinear model recently developed by Freilich & Guza (1984, hereinafter referred to as FG), was shown to be generally superior to LFDT for the prediction of frequency-band energy and phase (as measured by the coherence and phase between data and model). FG considered the shoaling of a spectrum of waves with a high-frequency cutoff $f = 0.234$ Hz, between depths of 10 and 4 m. The beach slope was $\beta = 0.022$. The present study extends the results of FG to water as shallow as 1 m, on a steeper beach ($\beta = 0.05$), to higher frequencies ($f < 0.4$ Hz), and considers some additional statistics (coherence between sensors, phase speed, skewness, and runs of high waves).

After a brief description of the experiment and data reduction, linear and nonlinear

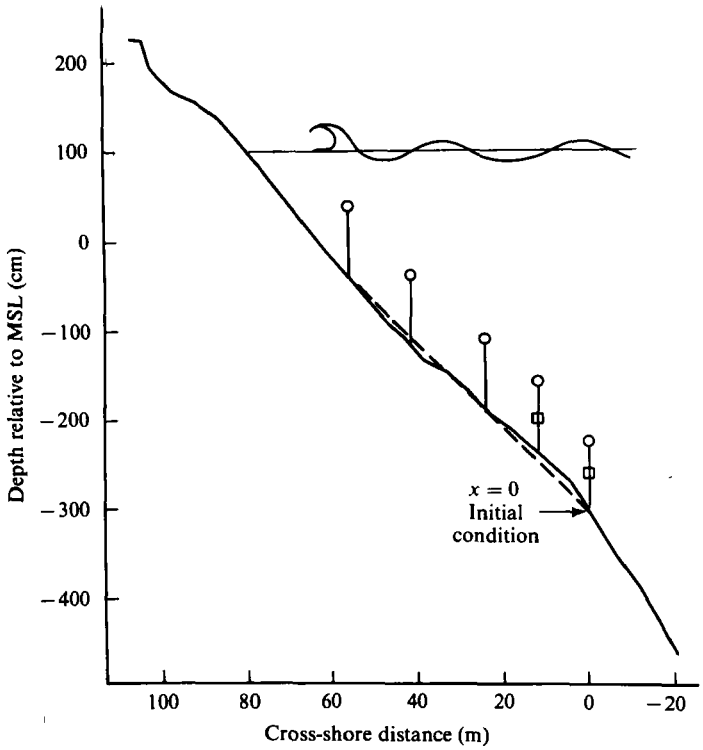

FIGURE 1. Measured beach profile, constant-slope approximation (dashed line), and instrument locations along a line perpendicular to the beach: ○, pressure gauges; □, bidirectional current meters.

models for the prediction of auto-spectra and cross-spectra (between two spatially separated sensors) are reviewed. The cross-spectral predictions are then used for comparison of models and observed coherences and phase speeds. Predictions of sea-surface-elevation skewness and the mean lengths of runs of high waves are also compared with observations. The results indicate that, for the statistics and wave conditions considered here, the nonlinear model is superior to LFDT. Finally, observations of directional spectra in 9 and 3–4 m depths indicate that nonlinear effects can be very important in the shoaling transformation of a directional spectrum.

2. Experiment

The field data were obtained at Santa Barbara, California, during the Nearshore Sediment Transport Study experiment conducted in January and February 1980 (Gable 1981). The observations used in the present study were obtained primarily from bottom-mounted pressure sensors, located along a line perpendicular to the beach (mean slope $\beta = 0.05$), from approximately 1–4 m depth (56 m horizontal distance). A typical beach profile and sensor locations are shown in figure 1.

Days with incident significant wave heights H_s (defined here as four times the sea-surface standard deviation) greater than 1 m are not considered because in those cases only a few pressure sensors were outside the surf zone, and the models examined in this study do not allow for wave breaking. In order to maximize the number of

Data set	Initial condition		Number of 512 s records	Most shoreward x-location (m) dissipation $< 15\%$
	Depth (cm)	H_s (cm)		
January 30	409	33	18	56
February 2	387	60	33	56
February 3	388	93	16	41
February 4	378	88	19	41
February 12	340	52	13	41

TABLE 1. Values of initial depth and significant wave height at the most seaward location (initial condition), number of 512 s records, and most shoreward x-location where dissipation is less than 15%

sensors available for model comparisons, five days with significant wave heights in the range 33–93 cm (table 1), and a variety of spectral shapes were selected. The zone of wave breaking is qualitatively indicated by the most shoreward location where the wave field's linear energy flux has decreased by less than 15% of the initial flux (table 1). The 30 January and 2 February data show no significant dissipation throughout the entire 56 m, while the other 3 data sets show a substantial decrease in energy flux between $x = 41$ m and $x = 56$ m.

The pressure gauges were sampled at 2 Hz for up to 5 h daily during the experiment. Bulk statistics (e.g. variance, frequency of the spectral peak, and various group statistics) were checked for stationarity. Data sets with any indication of non-stationarity were rejected. The selected data were processed by breaking the entire record into consecutive sections of 512 s each. After removal of tidal trends, linear finite-depth theory was used to convert Fourier coefficients of bottom pressure to sea-surface elevation (Guza & Thornton 1980 and references therein). A linear transformation is consistent with the lowest-order solutions to the Boussinesq equations (4.2). Finite-depth theory is used to avoid errors in the pressure-to-elevation transformation near the high-frequency cutoff ($f = 0.4$ Hz). With $A_1(\omega)$, $A_2(\omega)$ the complex Fourier coefficients observed at offshore locations x_1, x_2, the cross-spectrum (needed for coherence and phase-speed calculations discussed below) is

$$C_{12}(\omega) = Co(\omega) + \mathrm{i}\, Qu(\omega) = A_1(\omega)\, A_2^*(\omega), \tag{2.1}$$

with the real and imaginary parts the cospectrum and quadrature spectrum, respectively. The frequency resolution from the data (and for model initial conditions) is 1.95×10^{-3} Hz. Statistical stability is gained by averaging (cross-) spectra from many 512 s records and merging over neighbouring frequency bands, resulting in a final frequency resolution (for comparison between data and model predictions) of 7.8×10^{-3} Hz. Table 1 shows the number of 512 s sections for each data set, as well as the depth of water and significant wave height (H_s) at the deepest sensor (used as initial conditions for model predictions).

Bidirectional current meters colocated with the pressure sensors at $x = 0$ and $x = 12$ m were used to estimate the directional spectrum needed as input for LFDT coherence and phase predictions. Directional spectra at both locations were estimated with a maximum-likelihood technique (Oltman-Shay & Guza 1985) for each frequency band between 0.04 and 0.3 Hz. Because of low signal levels resulting from depth attenuation, directional spectra were not measured above 0.3 Hz. Directional spectra

for frequencies between 0.3 and 0.4 Hz were set equal to those measured at 0.3 Hz. Directional effects are not considered for frequencies below 0.04 Hz. Because of the small spatial separation, the directional spectra at $x = 0$ and 12 m differed primarily by a 5° rotation (which was independent of frequency and day). This discrepancy probably corresponds to errors in the current-meter orientation. A single directional spectrum representative of the input conditions was taken as the average of the $x = 0$ and 12 m spectra (corrected for the small rotation).

3. Linear finite-depth theory

The spectral transformation of a unidirectional, normally incident linear wave field is obtained by conserving energy flux, ECg = constant, where E is the energy and Cg is the group velocity. If each frequency component has a directional distribution of energy $S(\omega, \theta)$, LFDT takes a more complicated form. For plane, parallel contours (Le Méhauté & Wang 1982),

$$S(\omega, \theta) = \frac{k\,Cg_0}{k_0\,Cg} S_0\left[\omega, \sin^{-1}\left\{\frac{k}{k_0}\sin\theta\right\}\right], \tag{3.1}$$

where θ is the angle between the beach normal and a ray perpendicular to the wave crest, and the subscript zero refers to initial conditions. The wavenumber k is given by the finite-depth linear dispersion relation, $\omega^2 = gk \tanh(kh)$, where g is acceleration due to gravity and h is the depth. Thus, given an initial directional spectrum, $S(\omega, \theta)$ the directional spectrum at any other depth is determined. The energy at frequency ω is

$$E(\omega) = \int_0^{2\pi} S(\omega, \theta)\,\mathrm{d}\theta. \tag{3.2}$$

As mentioned above, data from pressure-sensor–current-meter pairs located at $x = 0$ and 12 m are used to estimate the initial directional distribution ($S_0(\omega, \theta)$) for an entire (i.e. all 512 s pieces) data set. When integrated over direction (3.2), $S_0(\omega, \theta)$ yields a band energy equal to that measured at the deepest sensor. Thus linear and nonlinear models both use the measured energy spectra at $x = 0$ m as initial conditions, but LFDT also uses the estimated directional distribution.

Substitution of $S_0(\omega, \theta)$ into (3.1) yields predictions of $S(\omega, \theta)$ at shoreward locations, which are in turn integrated, (3.2), producing predictions of power spectra. For a linear, random wave field with a directional distribution of energy, the complex cross-spectrum between two sensors with spatial separation Δx is (Munk, Snodgrass & Gilbert 1964; Yefimov, Solov'yev & Khristoforov 1972)

$$C(\omega) = Co(\omega) + \mathrm{i}\,Qu(\omega) = \int_0^{2\pi} \exp\{\mathrm{i}k\,\Delta x\cos\theta\}\,S(\omega, \theta)\,\mathrm{d}\theta. \tag{3.3}$$

4. Nonlinear model

Starting with the Boussinesq equations for a sloping bottom (Peregrine 1967), FG develop equations which describe the evolution of the wave field's Fourier amplitudes and phases owing to both shoaling and nonlinear effects. The model assumes that the waves are normally incident to a beach with plane-parallel contours, and that no energy is reflected or dissipated. The sea surface is represented as

$$\eta(t) = \sum_{n=1}^{N} a_n(x)\cos(\Phi_n(x) - \omega_n t), \tag{4.1}$$

where the radian frequency $\omega_n = n\Delta\omega$, with $\Delta\omega$ the radian-frequency resolution. At lowest order the waves are linear. The Fourier amplitudes a_n are spatially slowly varying. The spatial phase function Φ_n has both $O(1)$ derivatives (corresponding to the linear wavenumber) and higher-order derivatives which result in slow phase changes owing to nonlinear interactions. Substitution of (4.1) into the Boussinesq equations results in a set of coupled nonlinear differential equations for the amplitudes and phases. (See FG for a complete derivation and description of the dispersive nonlinear model.) Schematically, the differential equations are

$$\left.\begin{aligned} \dot{a}_n &= a_n S_n + \sum_j \tfrac{1}{4} a_j a_{n-j} R^{+}_{(j,n)} \sin(\Phi_j + \Phi_{n-j} - \Phi_n) \\ &\quad + \sum_j \tfrac{1}{4} a_j a_{j-n} R^{-}_{(j,n)} \sin(\Phi_j - \Phi_{n-j} - \Phi_n), \\ \dot{\Phi}_n &= k_n - \sum_j \left(\frac{a_j a_{n-j}}{a_n}\right) R^{+}_{(j,n)} \cos(\Phi_j + \Phi_{n-j} - \Phi_n) \\ &\quad + \sum_j \left(\frac{a_j a_{j-n}}{a_n}\right) R^{-}_{(j,n)} \cos(\Phi_j - \Phi_{j-n} - \Phi_n), \end{aligned}\right\} \tag{4.2}$$

with $k_n = (\omega_n/h^{\frac{1}{2}})(1 + \frac{1}{6}h\omega_n^2)$. The overdot indicates differentiation with respect to x, and the coupling and shoaling coefficients (R_n and S_n) are functions of ω and h (given explicitly in FG equations (21)–(24)). These equations can be numerically integrated given a set of initial amplitudes and phases. The approximations leading to the Boussinesq equations are not valid in deep or intermediate water depths, i.e. for depth-to-wavelength ratios which are not small. FG found good agreement between the nonlinear model and data for depths from 10 to 4 m, in the frequency range below 0.234 Hz. In the deepest water, the highest frequencies only marginally satisfied the shallow-water requirement. The present study, on a different beach, extends these results by using amplitudes and phases measured in 4 m depth as the initial conditions, and integrating the equations to depths as shallow as 1 m. This allows higher-frequency modes to be considered ($0.0 < f < 0.4$ Hz). On the other hand, another necessary assumption in deriving the nonlinear model is that the ratio of amplitude to depth be small. This assumption may start to break down in water as shallow as that considered here, and one purpose of the present work is to test the operational validity of the solutions for moderate amplitude-to-depth ratios.

For each 512 s record of data, Fourier coefficients of the deepest sensor were used as initial conditions for the numerical integration of (4.2), which yields predicted Fourier coefficients at shoreward locations. Many 512 s pieces were integrated and used to calculate predicted auto- and cross-spectra (2.1) with the same number of degrees of freedom as the observations.

5. Spectra

Measured energy spectra are compared to LFDT and nonlinear predictions at sensors shoreward of the initial conditions ($x = 0$ m) in figures 2–5. All the spectral (and coherence and phase speed) plots presented here have a frequency resolution of 0.0078 Hz. In the following discussion of power spectra (and coherence and phase speed) the data (except 12 February) will be examined in order of increasing energy, thus providing a sequence with increasing nonlinearity. The broad spectra on 30 January have the smallest waves considered ($H_s = 33$ cm), and there is very little spectral evolution as the wave field shoals (figure 2). The slight evolution that does

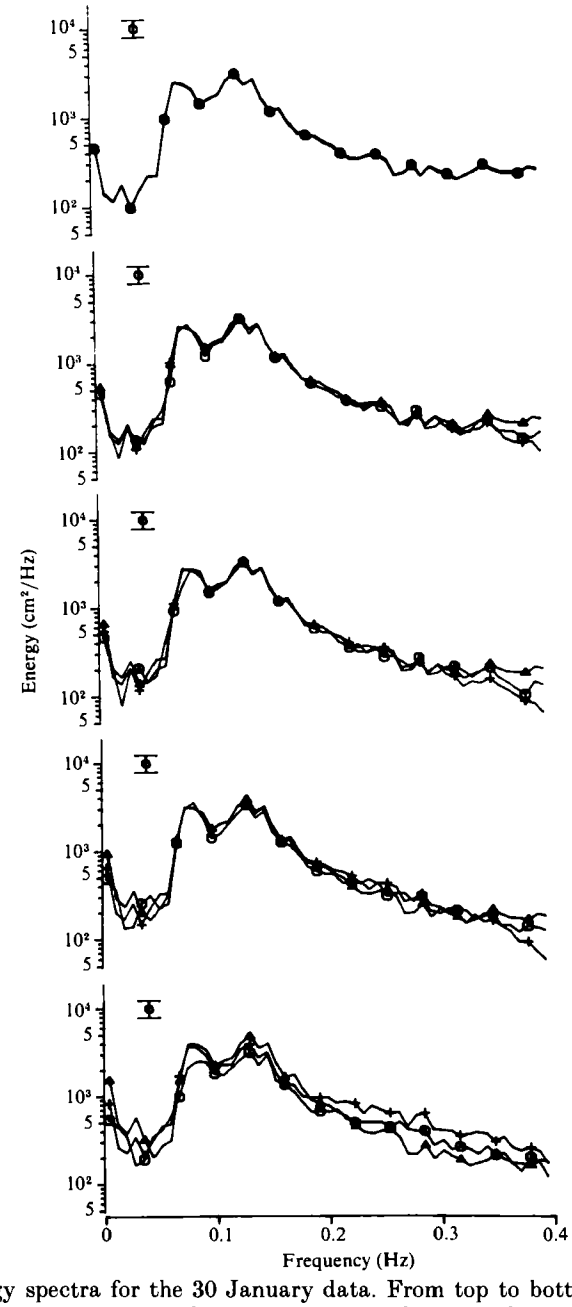

FIGURE 2. Energy spectra for the 30 January data. From top to bottom, $x = 0$ ($h = 4.1$ m), 12 (3.5 m), 24 (2.9 m), 41 (2.0 m), and 56 m (1.2 m). ○, data; ▲, directional LFDT; +, nonlinear model. There are 144 degrees of freedom (d.o.f.) and the bars indicate 95% confidence limits.

occur is modelled equally well by LFDT and the nonlinear model. Since this is an extremely low-energy wave field, it is not surprising that nonlinearities are not evident in the spectral evolution. Directional effects are of little consequence in LFDT energy spectra (in contrast to coherence and phase) predictions, so LFDT and the nonlinear model are essentially equivalent for 30 January. The narrowband spectra of 2 February (figure 3, $H_s = 60$ cm) show substantial spectral evolution. Harmonic

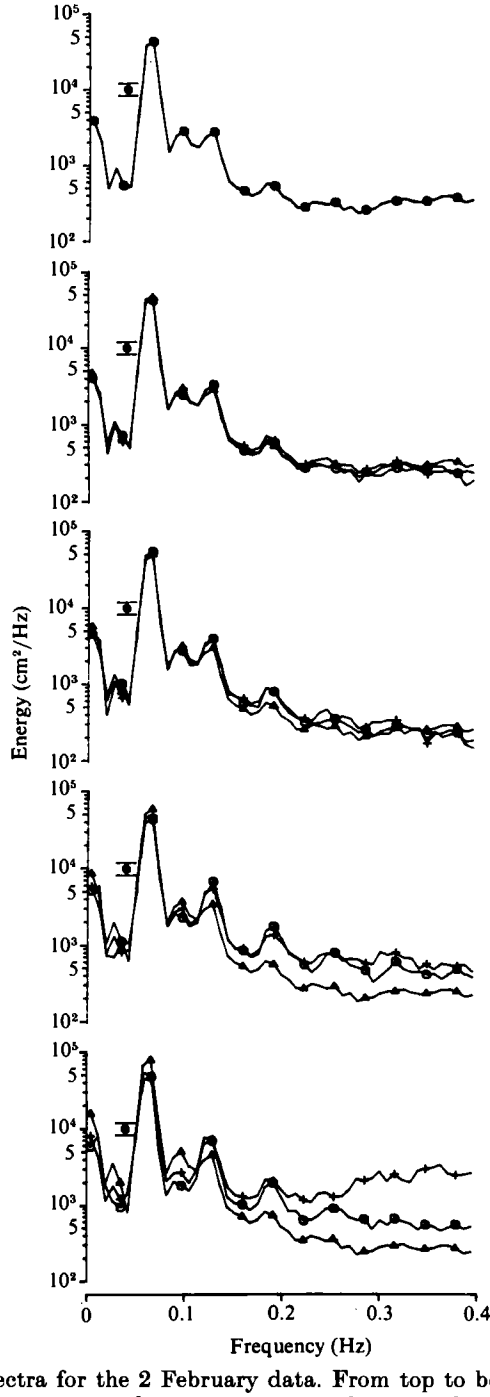

FIGURE 3. Energy spectra for the 2 February data. From top to bottom, $x = 0$ ($h = 3.9$ m), 12 (3.3 m), 24 (2.6 m), 41 (1.8 m), and 56 m (1.0 m). ○, data; ▲, directional LFDT; +, nonlinear model. There are 264 d.o.f., and the bars indicate 95% confidence limits.

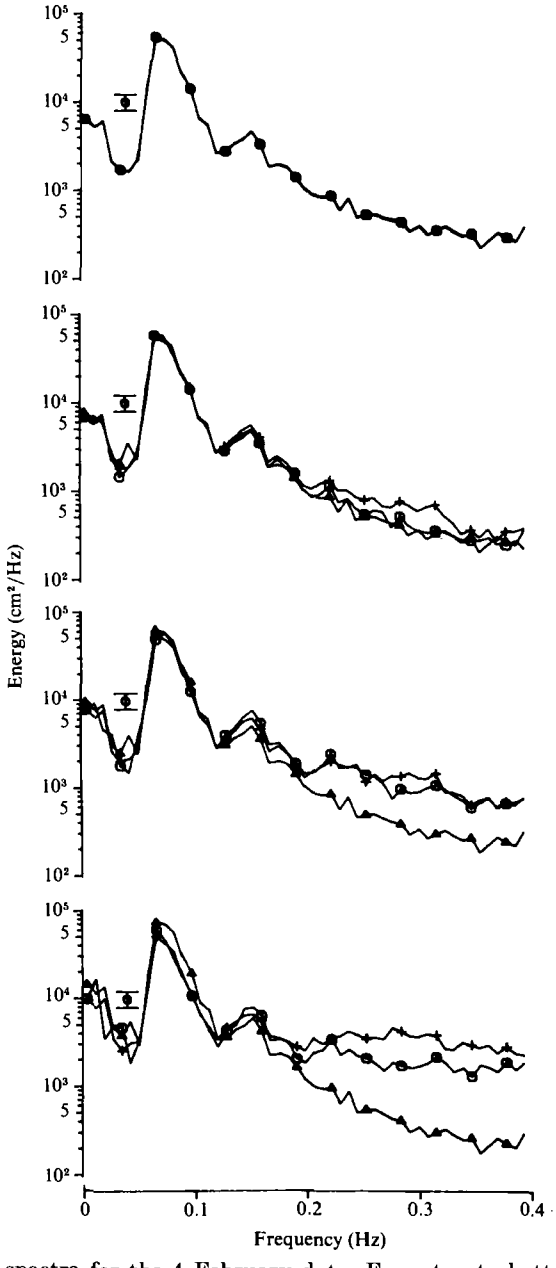

FIGURE 4. Energy spectra for the 4 February data. From top to bottom, $x = 0$ ($h = 3.8$ m), 12 (3.2 m), 24 (2.6 m), and 41 m (1.7 m). ○, data; ▲, directional LFDT; +, nonlinear model. There are 152 d.o.f., and the bars indicate 95% confidence limits.

($f = 0.12$, 0.18, 0.24 Hz) growth and an overall increase in high-frequency energy is accurately predicted by the nonlinear model for $x \leqslant 41$ m. At the most shoreward sensor, $x = 56$ m, the nonlinear model overpredicts spectral levels above 0.2 Hz. This is in part due to the existence of the high-frequency cutoff, $f = 0.4$ Hz. The nonlinear model enables energy to be transferred between modes, often from low frequencies to higher ones. For example, nonlinear interactions between the peak (0.06 Hz) and

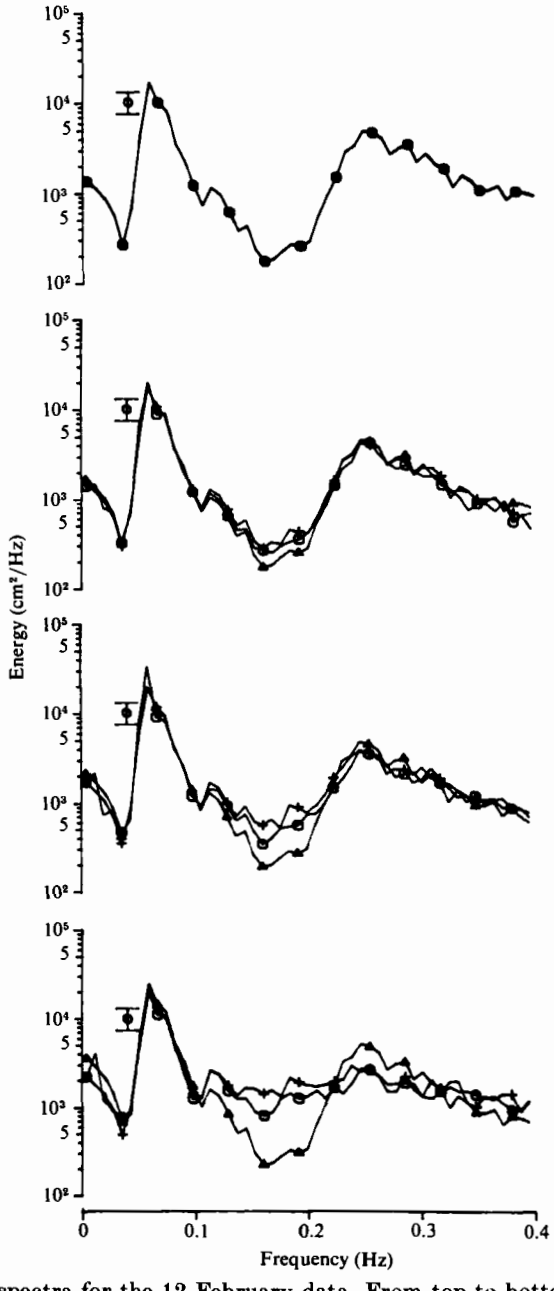

FIGURE 5. Energy spectra for the 12 February data. From top to bottom, $x = 0$ ($h = 3.4$ m), 12 (2.8 m), 24 (2.2 m), and 41 m (1.3 m). ○, data; ▲, directional LFDT; +, nonlinear model. There are 104 d.o.f., and the bars indicate 95% confidence limits.

its first harmonic (0.12 Hz) transfer energy to the second harmonic (0.18 Hz). Similar nonlinear interactions may require energy transfer to frequencies above 0.4 Hz, but these modes are prevented from receiving energy owing to the high-frequency cutoff. Model testing shows that energy builds up at those frequencies immediately below the cutoff frequency. The nonlinear equations were also integrated with identical initial conditions, but with a high-frequency cutoff at 0.234 Hz. For these conditions,

the nonlinear model predicted spectral evolution accurately as far as $x = 41$ m. However, as in the higher-frequency-cutoff case, at $x = 56$ m the model overpredicted spectral levels just below the cutoff frequency, from about 0.18 to 0.234 Hz. Another possible contribution to the model's overprediction of high-frequency energy at $x = 56$ m is that in water this shallow (less than 1 m) the ratio of amplitude to depth ($H_{\rm rms}/2h = 0.25$) may not be small enough to satisfy the assumptions made in deriving the nonlinear model. Finally, there is some dissipation by $x = 56$ m, although it is less than 15 %. It is unknown how wave-breaking affects the spectrum, but in any case the nonlinear model does not account for dissipation. Comparisons of spectra from colocated surface-piercing wave staffs and pressure sensors in relatiyely shallow water (Esteva & Harris 1970; Guza & Thornton 1980; and others) suggest that the conversion from pressure to sea-surface elevation is not responsible for the high-frequency discrepancies.

Although the 4 February spectra have shapes (figure 4) similar to the 2 February data (figure 3), the former is substantially more energetic ($H_{\rm s} = 88$ cm). Consequently, nonlinearities are stronger, amplitude evolution is more rapid, and nonlinear spectral evolution is significant by $x = 24$ m (compare 4 February at $x = 24$ m, figure 4, with 2 February at $x = 24$ and $x = 41$ m, figure 3). In addition, the nonlinear model begins to overpredict high-frequency ($f > 0.2$ Hz) spectral levels at $x = 41$ m ($H_{\rm rms}/2h = 0.2$). Because there is substantial dissipation between $x = 41$ and 56 m on 4 February, the $x = 56$ m data are not shown. The 3 February data set (not shown) has spectra which are similar in shape and level to those of 4 February, and comparable agreement between model predictions and data.

The 12 February spectral shape (figure 5) differs from the previously discussed data sets (figures 2–4). The double-peaked spectra represent a combination of a narrow swell peak, centred at $f = 0.07$ Hz, and a broad sea peak above $f = 0.24$ Hz. As the waves shoal, the measured high-frequency ($f > 0.24$ Hz) energy is seen to decrease below LFDT predictions while the spectral valley ($f \approx 0.15$ Hz) separating the peaks rises above LFDT values. As predicted by the nonlinear model, energy apparently is being transferred from both low- and high-frequency peaks to the mid-frequency valley.

6. Coherence and phase speed between sensors

The objective of this section is to address the relative accuracy of LFDT and nonlinear model predictions of the phase evolution of shoaling waves in shallow water. There are several ways to accomplish this; for example, predicted and observed cross-spectra (between sensors) could be directly compared. However, the most commonly used approach is to recast the cross-spectrum into coherence and phase speed. To facilitate comparison with previous work, this is also done here. Coherence squared and phase speed are defined in (6.1) and (6.2), respectively:

$$COH^2 = \frac{Co(\omega)^2 + Qu(\omega)^2}{C_{11}C_{22}}; \tag{6.1}$$

$$C_{\rm p} = \frac{\omega \Delta x}{\phi(\omega)}, \tag{6.2a}$$

where $\phi(\omega)$, the phase difference between sensors, is given by

$$\phi(\omega) = \arctan\left(\frac{Qu(\omega)}{Co(\omega)}\right). \tag{6.2b}$$

LFDT predictions of $Co(\omega)$ and $Qu(\omega)$ are obtained from (3.1) and (3.3), given an initial directional spectrum $S_0(\omega, \theta)$. Nonlinear cross-spectral predictions are calculated from the predicted Fourier coefficients at the appropriate locations. Another common definition of phase speed is (Yefimov *et al.* 1972; Huang & Tung 1977)

$$C_p(\omega) = \frac{\omega \int_0^{2\pi} S(\omega, \theta)\, d\theta}{\int_0^{2\pi} k \cos\theta S(\omega, \theta)\, d\theta}. \tag{6.3}$$

These two definitions ((6.2) and (6.3)) for phase speed are equal if the waves are unidirectional or if the sensor separation is small, such that $k\Delta x \ll 1$ (Yefimov *et al.* 1972; Huang 1981). However, (6.2) and (6.3) are not, in general, the same. Consequently, it is inappropriate to compare phase speeds obtained from data using (6.2) with theoretical phase speeds calculated with (6.3). For this study, (6.2) is used exclusively. Although Huang (1981) and others consider (6.3) to be the 'true answer' for phase speed, there is no obvious justification for this assertion. Neither of these definitions ((6.2) or (6.3)) appears in a fundamental theoretical way. It is only necessary that the definition of phase speed used for theoretical calculations is the same as that used for data-based computations.

Theoretical and observed coherence and phase-speed spectra are shown in the upper and middle panels of figures 6–8 for 30 January, 2 February, and 4 February (with H_s = 33, 60, 88 cm respectively). The two solid lines in each phase-speed plot are theoretical linear values of celerity. The lower line is the phase speed predicted by the linear finite-depth dispersion relationship assuming a normally incident wave field, while the upper line is the theoretical linear phase speed calculated with directional effects ((3.1) and (3.3)). To apply (3.3), a flat bottom was assumed, with depth equal to the mean depth of water between the two sensors. Accounting for the (small) depth variation produces negligible differences. Because mean cross-shore currents in the field data were a very small fraction of the observed phase speeds, Doppler shifts are assumed to be zero. The observed power spectra for each sensor used in the corresponding coherence and phase plots are shown in the lower panel. The present discussion considers only frequencies above f_p, the frequency of maximum power (indicated with a vertical arrow). Lower frequencies are considered later.

Recall that LFDT power-spectral predictions are relatively insensitive to directional effects. Therefore the similarity of nonlinear and LFDT power-spectra predictions on 30 January suggested that nonlinear effects were weak for $x \leqslant 41$ m (figure 2). This is confirmed by the general similarity of nonlinear (which assumes normal incidence) and normally incident LFDT phase-speed predictions (figure 6). The differences at the highest frequencies at the deepest sensor pair shown (figure 6*a*) are consistent with the linear Boussinesq dispersion relationship of the nonlinear model, which underpredicts phase speed for components if kh is not small, as described in detail in FG. Directional effects are most apparent at the two deepest sensor pairs (figures 6*a* and *b*), where the observed coherences at frequencies above f_p are more accurately modelled by directional LFDT. Some of the tendency towards non-dispersiveness in figures 6 (*a*) and (*b*) is, according to these calculations, a linear effect associated with the observed wider directional distributions at high frequencies.

As the waves shoal (figure 6*b*) several effects become apparent. The difference between directional and normally incident LFDT phase speed diminishes, in accordance with refractive narrowing of the directional spectrum. Also, as kh becomes

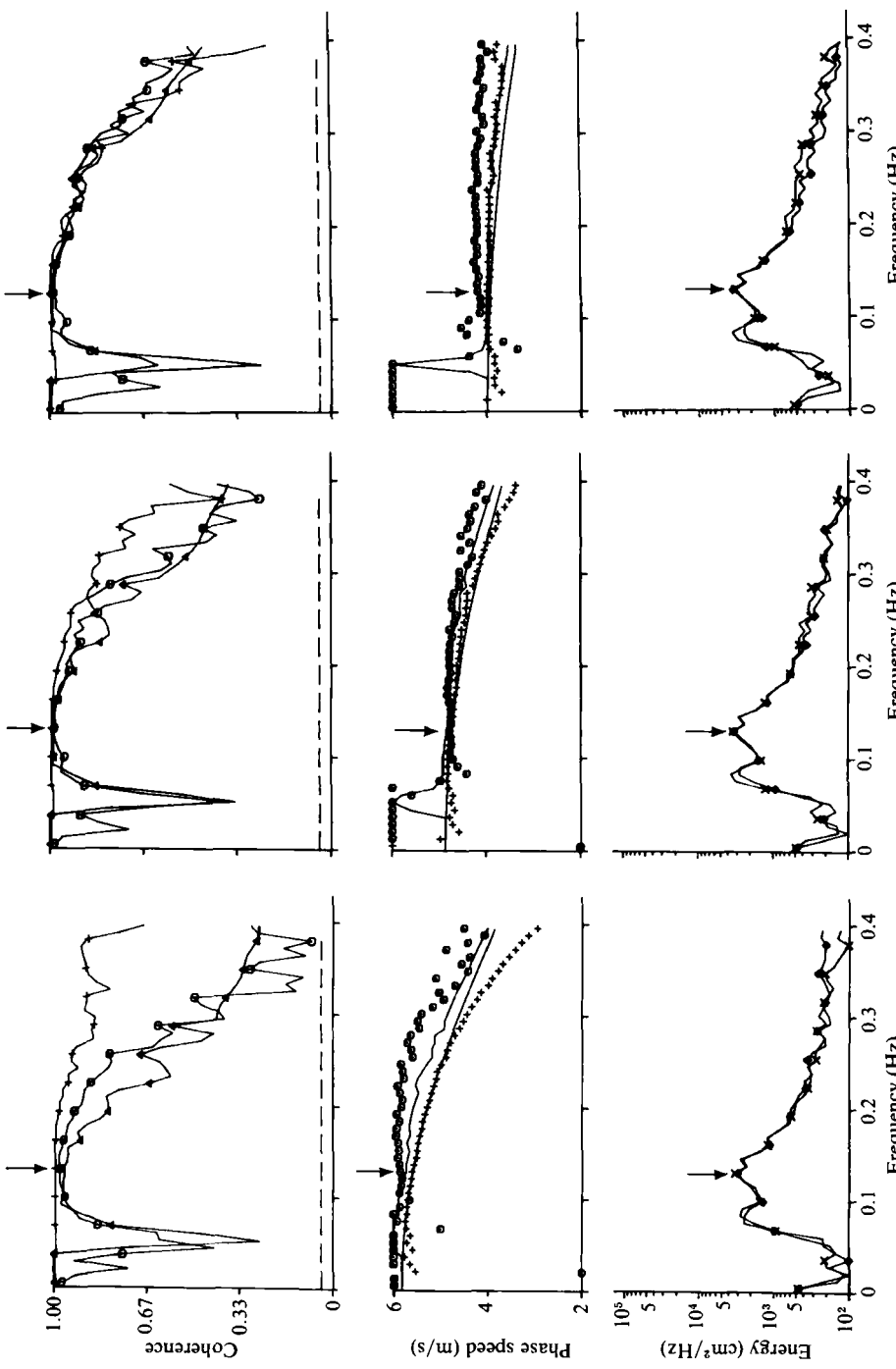

FIGURE 6. Coherence between sensors (top), phase speed (middle) and power spectra of field data (bottom) *versus* frequency for 30 January, 144 d.o.f. Coherence symbols: ○, data; ▲, directional LFDT; +, nonlinear model. Normally incident LFDT coherence is 1.0 (not shown). Phase-speed symbols: ○, data; +, nonlinear model; upper solid line, directional LFDT; lower solid line, normally incident LFDT. Phase speeds greater than 6 m/s are set equal to 6 m/s for plotting purposes. Power-spectra symbols: ◆, deeper sensor; ×, shallower sensor. (*a*) $x = 0$ and $x = 24$ m; (*b*) 24 and 41 m; (*c*) 41 and 56 m. The dashed line indicates 95% confidence of zero coherence. Vertical arrows indicate the frequency with maximum power.

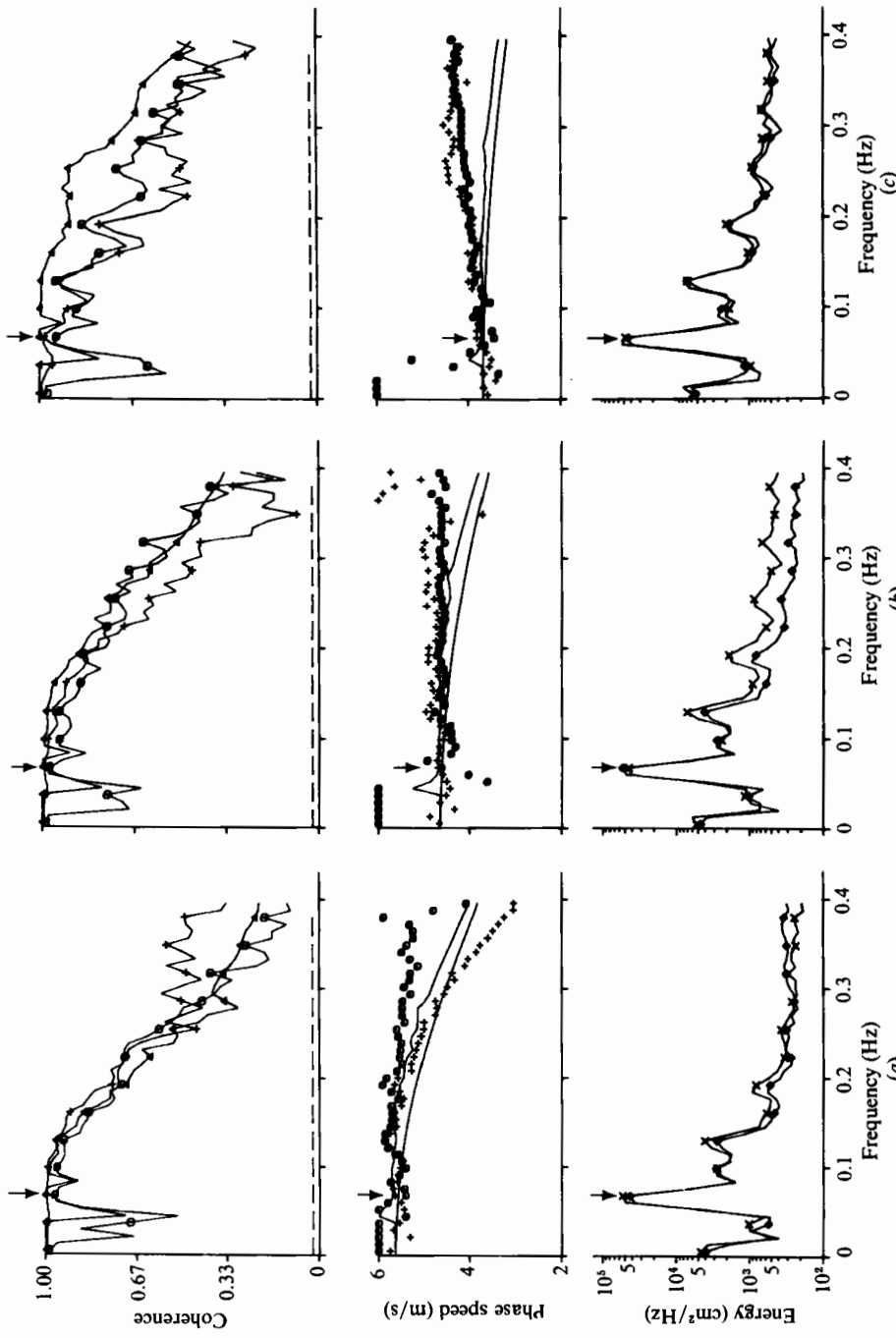

FIGURE 7. Same symbols as figure 6, but for 2 February data, 264 d.o.f.
(*a*) $x = 0$ and $x = 24$ m, (*b*) 24 and 41 m, (*c*) 41 and 56 m.

smaller the linear Boussinesq dispersion relationship is more accurate, and the high-frequency nonlinear-model values of phase speed approach normally incident linear theory. At the shallowest sensor pair (figure 6*c*) refraction has further reduced the difference between directional and normally incident LFDT phase speeds, while nonlinear interactions have raised nonlinear-model phase speeds slightly above normally incident LFDT predictions. The data in figure 6(*c*) have phase speeds slightly above all the predictions, suggesting that directional and nonlinear effects are of comparable (small) magnitude, and both contribute to the observed increase in phase speed. Perhaps coincidentally, the predicted nonlinear and directional LFDT coherence values at the shallowest station are virtually identical, and both compare favourably with the data.

As expected, the larger wave height on 2 February ($H_s = 60$ cm compared with $H_s = 33$ cm on 30 January) results in stronger nonlinearities. At the deepest sensor pair (figure 7*a*), below about 0.20 Hz the nonlinear-model phase speeds show exceptionally good agreement with the data. Frequencies which are harmonics of f_p have phase speeds larger than directional LFDT while the phase speeds of some non-harmonic frequencies are actually decreased. Above 0.20 Hz the nonlinear predictions of phase speed fall below LFDT (and the data) because of the inaccuracy of the linear Boussinesq dispersion relation when kh is not small. In shallower water, however, the nonlinear model predicts the observed phase speeds out to the highest frequencies investigated (figure 7*b* and *c*), while LFDT theories underpredict the observations over most of the frequency range. It is interesting to note that the observed and nonlinearly predicted phase speeds are actually increasing with frequency. In very shallow water, LFDT coherence predictions are too high, while the nonlinear model has coherence values close to the data, with local maxima at frequencies corresponding to the second and third harmonics of the spectral peak (figure 7*c*).

Coherences and phase speeds between the two most offshore pairs of sensors on 4 February, a data set with spectral shape similar to 2 February but with 50 % larger incident wave heights ($H_s = 88$ cm), are shown in figure 8. Perhaps fortuitously, the nonlinearly predicted phase speeds do not show the effects of linear Boussinesq dispersion even at the deepest sensor pair (figure 8*a*), and the nonlinear model accurately predicts observed phase speeds at all frequencies. As described by (4.2), increasing the wave height increases the rate of nonlinear phase evolution (compare figure 7*b* with figure 8*a*). At the next sensor pair shoreward ($x = 24$ and 41 m, figure 8*b*), the nonlinear-model predictions of phase speed have a structure similar to the data, with local maxima at harmonics of the spectral peak, but are offset by about 0.6 m/s at all frequencies above f_p. The measured mean offshore current between these sensors, approximately 0.13 m/s (two to three times higher than the corresponding mean currents on 30 January, 2 February, and 12 February) can account for only about 25 % of the offset. Coherence and phase speed for 3 February (not shown) are similar to those of 4 February.

Comparisons of observed and LFDT coherences and phase speeds require specification of the directional spectrum ((3.3), (6.1) and (6.2)). It does not seem to be universally appreciated that coherence and phase speed are calculated using elements of the same cross-spectral matrix which is the fundamental information used in estimating the directional spectrum from observations (Barber 1963). Given a linear wave field and an array of sensors, an ideal directional-spectrum estimator yields directional spectra which are as consistent as possible with the measured cross-spectra, and hence with the observed coherence and phase speed between all sensor

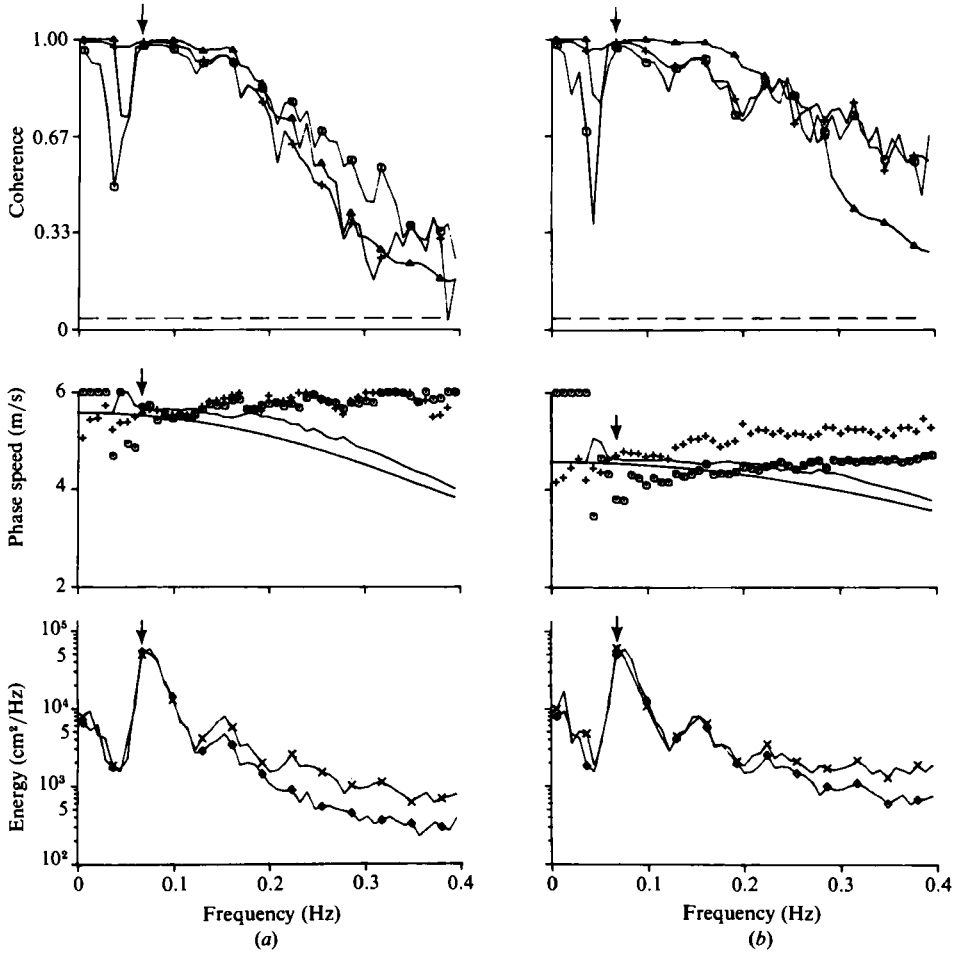

FIGURE 8. Same symbols as figure 6, but for 4 February data, 182 d.o.f. (*a*) $x = 0$ and $x = 24$ m (*b*) 24 and 41 m.

pairs. On the other hand, if a standard low-resolution directional estimator is used, or an arbitrary directional form (such as $S(\omega, \theta) = \cos^n(\theta - \theta_0)$) is assumed, then theoretical (LFDT) and observed phase speeds will not agree even if the wave field is linear.

In the field observations of Yefimov *et al.* (1972), high-frequency waves had phase speeds between the free-wave speed and the speed of the spectral peak. Yefimov *et al.* (1972) suggested that free and forced components are both significant in these data, but the data are also consistent with free waves alone. To resolve the ambiguity an extensive two-dimensional array would be required to map accurately the high-frequency energy distribution in (ω, $\boldsymbol{k}$) space, and thereby quantify the relative amounts of free and forced waves contributing to the observed phase speeds.

In a homogeneous ocean it is not possible to separate directional-spectra measurements from observations of coherence and phase speed. Note that in the present experiment coherence and phase speed are examined at sensors other than those used to estimate the directional spectra. The directional estimates at $x = 0$ m are used as initial conditions in order to study the propagation of directional LFDT through an inhomogeneous field (the shoaling region). Thus the somewhat circular comparisons

discussed above are avoided. However, there are fundamental problems in estimating the directional spectra with a pressure-sensor–current-meter system (or slope array, or pitch-and-roll buoy) if the wave field is not linear. In this case, any directional estimate which relies on linear theory is itself corrupted to some degree. The directional spectra at $x = 0$ and 12 m were calculated with several different (but formally equivalent) linear assumptions, with no substantial difference in the results. Thus the estimated directional spectra are considered to be not distorted strongly by the use of linear theory. This conclusion is also supported by the nonlinear-model dynamics. To lowest order all waves (even if nonlinearly generated) follow the linear Boussinesq dispersion relation. Unlike the deep-water case, departures from the linear dispersion relation are never large.

The discussion above has considered the coherence and phase speed of frequencies at or above f_p. The observations below f_p, which are now briefly considered, are quite different (figures 6–8). The phase speeds are erratic, with values both substantially above and below the phase speeds for components above f_p. Linear outgoing (i.e. reflected) waves qualitatively explain these observations. Consider a wave field consisting of a normally incident linear wave and its phase-locked reflection

$$\eta = a\cos\left(\int k\,\mathrm{d}x + \omega t\right) + Ra\cos\left(\int k\,\mathrm{d}x - \omega t\right), \tag{6.4}$$

where R is the reflection coefficient. On a flat bottom, in very shallow water the cross-spectrum is given by

$$\left.\begin{aligned} Co^2(\omega) &= (1+R)^2\cos(kx)\cos(k(x+\Delta x)) + (1-R)^2\sin(kx)\sin(k(x+\Delta x)),\\ Qu^2(\omega) &= -(1-R)^2\sin^2(k\,\Delta x), \end{aligned}\right\} \tag{6.5}$$

where $k = \omega/(gh)^{\frac{1}{2}}$ and Δx is the sensor separation.

When $R = 0$ the associated phase speeds are equal to $(gh)^{\frac{1}{2}}$. When $R = 1$, the phase difference is zero between sensors which are not separated by a zero crossing of the standing wave. The phase speed is then infinite. Sensors which are separated by a zero crossing are π out of phase, independent of the sensor separation. Very closely spaced sensors which happen to be separated by a zero crossing will yield a phase speed close to zero. Thus phase speeds of any magnitude can occur with a pure standing wave. Note that this result does not follow from (3.3) with a directional spectrum consisting of two waves travelling in opposite directions. Equation (3.3) is valid for spatially homogeneous wave fields such as occur when waves travelling in different directions are phase independent. If a relatively narrow bandwidth in frequency is considered, close to a reflector (e.g. the beach), then incoming and outgoing waves are phase coupled. Suhayda (1974), Holman (1981), and others have shown clear evidence that low-frequency ($f < f_p$) 'surf beat' energy near beaches occurs in the form of waves standing in the cross-shore. Guza & Thornton (1985*b*) have shown similar results for the present data set. The observed phases (figure 9*c*) suggest that the lowest-frequency waves are almost completely reflected, while the highest-frequency waves are primarily progressive. The lower two panels of figure 9 are phase speeds and phases calculated using (6.5), with

$$R = \left\{\begin{array}{ll} \left(1-\dfrac{f}{f_p}\right)^2 & \text{if } f < f_p,\\ 0 & \text{if } f > f_p, \end{array}\right\} \tag{6.6}$$

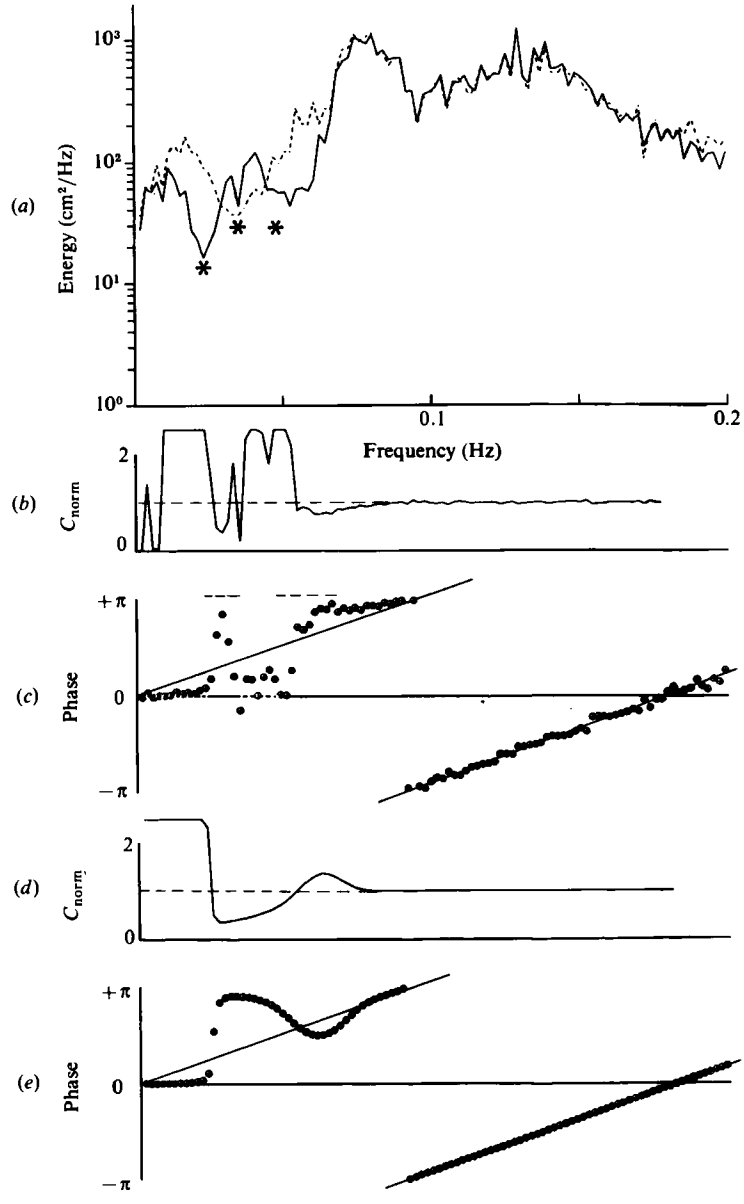

FIGURE 9. (*a*) Power spectra, (*b*) phase speed (normalized by $(gh)^{\frac{1}{2}}$), values of normalized phase speed greater than 2.25 have been set equal to 2.25 for plotting purposes, and (*c*) phase difference observed on 30 January with pressure sensors at $x = 41$ and $x = 62$ m, mean depth = 1.5 m. The asterisks on the power spectra indicate predicted standing-wave nodal locations (Guza & Thornton 1985*b*). The centre asterisk is for $x = 62$ m (dashed line); the other two are for $x = 41$ m (solid line). Spectral minima do indeed occur near these locations. The dashed line in the observed phase spectra (*c*) indicates the phase values which would occur if the waves are purely standing. The solid sloping lines are the phase differences if the linear waves are purely progressive. (*d*) Normalized phase speed and (*e*) phase difference predicted by reflected-wave model, equations (6.5), (6.6).

where $f_p = 0.08$ Hz. This form for the reflection coefficient was selected arbitrarily, and no attempt was made to alter it to fit the data better. The point is that the observed and model ((6.5) and (6.6)) phase speeds exhibit qualitatively similar behaviour. The 'anomalous' phase speeds observed at low frequencies near a coast by Büsching (1972) are probably due to standing waves. Laboratory experiments might also show this effect. Certainly, observations of low-frequency phase speeds less than linear values (Ramamonjiarisoa & Coantic 1976) do not necessarily 'contradict the established characteristics of water wave motion' as asserted by Huang & Tung (1977).

In the open ocean, there is no phase coupling between different directions and (3.3) is valid. In this case coherence is decreased and phase speed increased by energy propagating opposite to the main wave direction. Equation (3.3) predicts a decrease in coherence as large as 20% and a 20% increase in phase speed caused by an oppositely propagating wave having 10% of the energy of the main wave. Many deep-water investigations have assumed directional spectra with little or no energy at angles greater than 90° from the direction of the directional spectrum's peak. On the other hand, Munk *et al.* (1963) and Snodgrass *et al.* (1966) present evidence indicating the existence of a background-radiation field in the ocean. Although this isotropic radiation may be low in energy, it can conceivably have an effect comparable to nonlinearities.

7. Skewness

For a zero-mean process the skewness is defined as

$$\text{skewness} = \frac{\mathrm{E}|\eta^3|}{\mathrm{E}|\eta^2|^{\frac{3}{2}}}, \tag{7.1}$$

where E is the expected value, or average, operator. A sea surface composed of a linear combination of sinusoids with random phases has (statistically) zero skewness. On the other hand, it is well known that measured values of skewness in the shoaling region are, on average, greater than zero, consistent with the observation that the waves have sharp peaks and broad, flat troughs. Sea-surface skewness has been observed to evolve from a value close to zero in deep water to a maximum somewhat seaward of the region of breaking, and finally decreasing in shallower water (Guza & Thornton 1985*a*). Similar skewness evolution was observed in the data investigated in the present study (figure 10). Skewness was calculated by averaging the skewness (7.1) from successive 512 s records of band-passed ($0.04 < f < 0.3$ Hz) sea-surface elevation and cross-shore velocity. The velocity skewnesses are included to illustrate qualitatively that their evolution is similar (with the exception of 12 February data) to sea-surface skewness. In a non-dispersive, shallow-water theory, these skewnesses are, in fact, equal. The higher-energy wave fields tend to have higher maximum values of skewness (figures 10*c*, *d*) than the low-energy waves (figures 10*a*, *b*, *e*). (The spectra for 3 February, not shown, are similar in shape and level to the 4 February data, figure 4). At 4 m depth ($x = 0$ m, initial condition) the low-energy data (figures 10*a*, *b*) are in the increasing stage of skewness evolution, while the higher-energy data (figures 10*c*, *d*) are near or beyond the peak skewness value. The double-peaked spectra of 12 February (figure 5) have different observed skewness evolution, with observed sea-surface skewness values close to and below zero (figure 10*e*).

The nonlinear model predicts observed trends in skewness evolution for four of the five data sets. The anomalous behaviour of 12 February data is not predicted by the

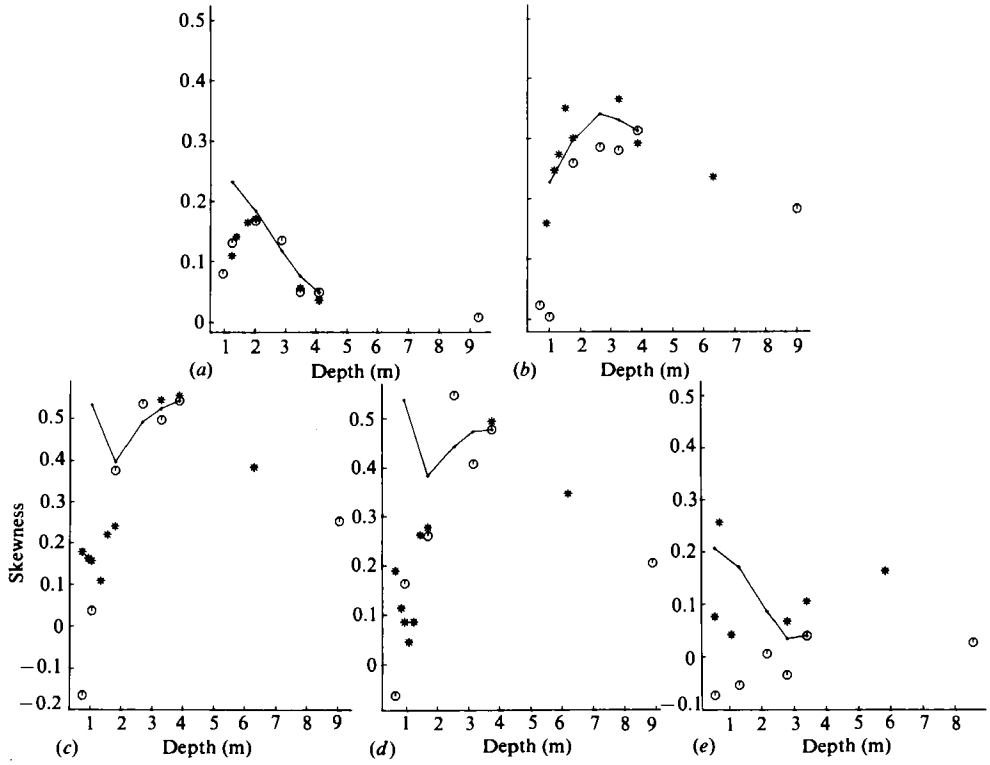

FIGURE 10. Skewness *versus* depth: ○, observed sea-surface-elevation skewness; *, observed cross-shore-velocity skewness; +, sea-surface-elevation skewness predicted by the nonlinear model, equation (4.2). The solid connecting line is a visual aid. (*a*) 30 January, $H_s = 33$ cm; (*b*) 2 February, 60 cm; (*c*) 3 February, 93 cm; (*d*) 4 February, 88 cm; (*e*) 12 February, 52 cm.

nonlinear model. Some of the data sets show substantial dissipation by the most shoreward sensor (table 1) owing to wave breaking. Although it is not theoretically known how the skewness of a broadband wave field is affected by dissipation, it appears that for those data considered here wave breaking is associated with a large decrease in skewness. The comparison between data and nonlinear predictions indicates that the nonlinearities modelled by (4.1) are governing skewness evolution in the shoaling region, at least for $x \leqslant 41$ m. The upturn in nonlinear-model skewness predictions at $x = 56$ m for 3 and 4 February (figures 10*c*, *d*) may be due to the over-prediction of energy levels at high frequencies ($f > 0.2$ Hz) by the nonlinear model, as discussed above (figures 3, 4). A detailed investigation of skewness evolution through the shoaling region and the surf zone using bispectral techniques is in progress.

8. Wave groups

Wave-group statistics observed in approximately 10 m depth during the Santa Barbara experiment were shown by Elgar *et al.* (1984) to be not inconsistent with linear dynamics. On the other hand, group statistics observed in shallower water (< 4 m) showed marked departure from linear theory. One such wave-group statistic is the mean length of runs of consecutive waves which exceed the significant wave height.

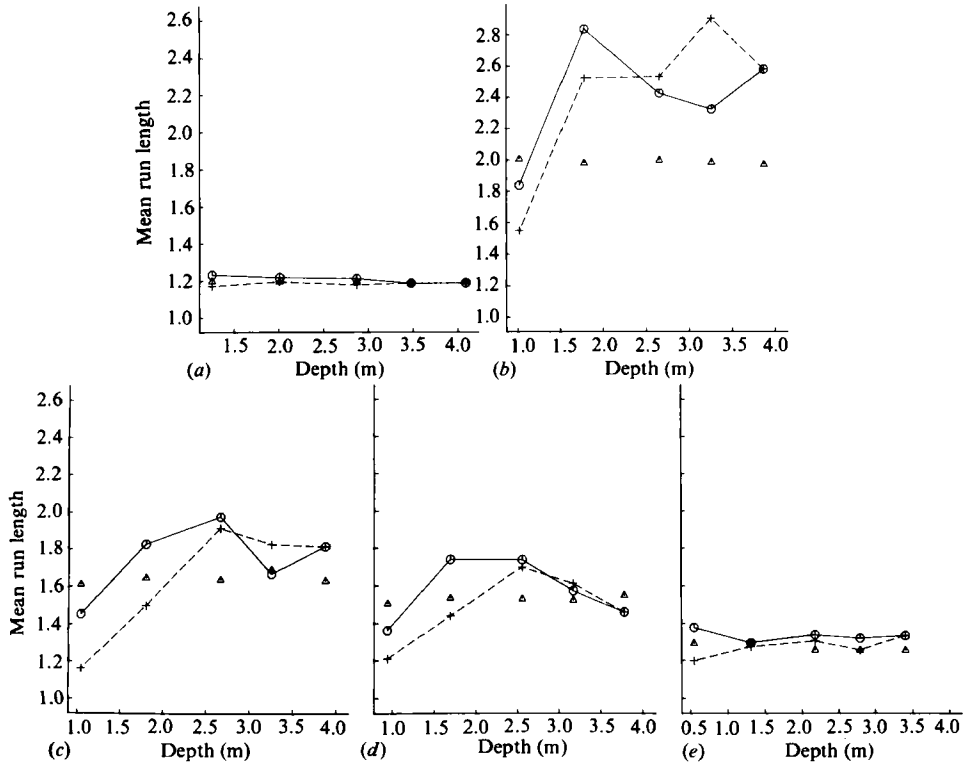

FIGURE 11. Mean length of runs greater than the significant wave height *versus* depth. ○, data; △, directional LFDT; +, nonlinear model. The solid and dashed lines are a visual aid. (*a*) 30 January; (*b*) 2 February; (*c*) 3 February; (*d*) 4 February; (*e*) 12 February.

In the light of Elgar *et al.* (1984), it is interesting to compare observations of mean run lengths with linear and nonlinear predictions, as in figure 11. Linear predictions of run lengths at each sensor location were obtained from time series associated with spectra calculated from (3.1). The spectra were band-pass filtered ($0.04 < f < 0.3$ Hz), coupled with random phases, and subjected to inverse fast Fourier transformation to yield a time series with the desired linearity. This process was repeated 100 times at each sensor location for each data set. The LFDT run lengths shown in figure 11 are averages of mean run lengths from the 100 realizations. Details of the simulation procedure and of the statistical behaviour of run lengths can be found in Elgar *et al.* (1984). As shown in figure 11, the mean run lengths predicted by LFDT are substantially different from those observed in the field data at the deepest sensor for several of the data sets, indicating that some of the 4 m data are inconsistent with random phases. However, the linearly predicted run length in 4 m for the low-energy 30 January data is almost identical with the field value (figure 11*a*). As the 30 January data show, the run lengths remain almost constant, and are predicted almost equally well by both LFDT and the nonlinear model. The 12 February data (figure 11*e*) also have a fairly constant mean group length throughout the shoaling region, which is predicted only slightly more accurately by the nonlinear model than by LFDT. In contrast to the nearly constant mean run lengths of 30 January and 12 February, the 2, 3, and 4 February data (figures 11 *b–d*) show substantial run-length evolution, with an increase in run length between 4 and

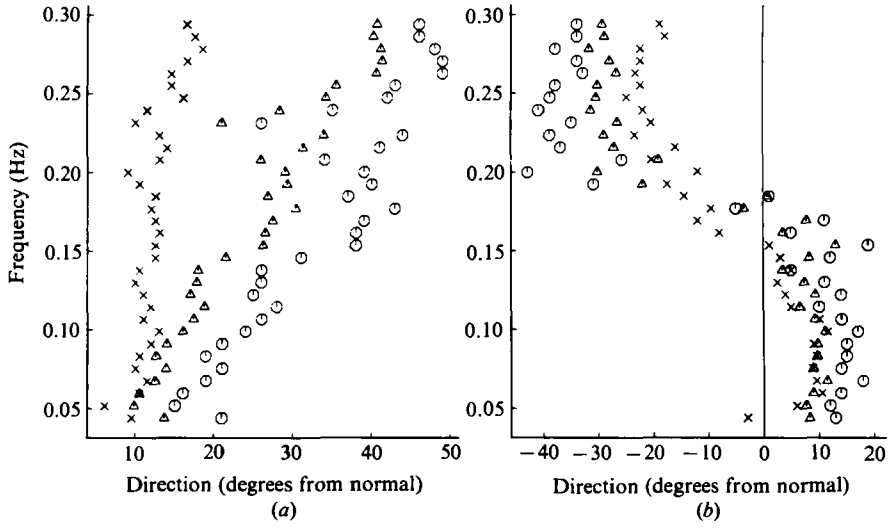

FIGURE 12. Direction, relative to the beach normal, of the peak of the directional spectra for each frequency band. ○, angle measured in 9 m depth; △, angle predicted by Snell's law in 3–4 m depth; ×, angle measured in 3–4 m depth. (*a*) 2 February; (*b*) 12 February.

2 m depths, and then a sharp drop in run length in shallower water. The linear-theory predictions do not model this behaviour at all, displaying a relatively constant value of run length throughout the entire region. The nonlinear model, however, does predict the structure of run-length evolution for these three data sets, with the predicted mean length of runs rising above the initial values and then dropping to a low value in shallower water.

9. Discussion

Directional spectra in 9 m depth were obtained from a slope array of 4 bottom mounted pressure sensors, which contains information formally equivalent to the colocated pressure-sensor–current-meter pairs used in shallower water. Like the 3–4 m directional spectra, the 9 m-depth directional spectra were calculated with a maximum-likelihood technique (Oltman-Shay & Guza 1985). Figure 12 shows the measured 9 m-depth central angle (angle of maximum power) as a function of frequency, along with the central angle predicted by Snell's law in shallow water (approximately 3.5 m, depending on tidal stage), and the angle actually measured at the shallow depth. Plane-parallel contours were assumed. Linear refraction using the actual topography makes only a few degrees difference to the predicted shallow-water angles of 0.1 and 0.2 Hz plane waves. Snell's law accurately predicts the shallow-water central angle for $f < 0.1$ Hz, but not for higher frequencies, with discrepancies as large as 30°. The measured high-frequency central angles in shallow water tend toward alignment with the spectral peak's direction, which is nearly normally incident.

These results are consistent with the (nonlinear) generation of a high-frequency directional mode aligned with the low-frequency peak, as observed by FG with linear arrays in 10 and 4 m depths, if the limited resolution of the directional estimates in the present study is taken into account. The pressure-sensor–current-meter system cannot resolve peaks separated by less than 60°, and gives a central angle skewed

toward the more energetic mode (Oltman-Shay & Guza 1985). Thus, the 2 February directional spectra (figure 12*a*), which show the entire high-frequency band to be almost colinear with the low-frequency swell peak, suggest that most of the high-frequency energy at 4 m is nonlinearly generated shoreward of the 9 m station. In contrast, the high-frequency central angles in 4 m depth on 12 February (figure 12*b*) are displaced by only about one-third of the angular spread between the predicted Snell's law angles and the low-frequency peak. This is consistent with a smaller fraction of the 12 February high-frequency energy in 4 m depth being nonlinearly generated, as would be expected given the approximately equal amounts of energy in high- and low-frequency bands (figure 5). It is noteworthy that the observed low-frequency angles in 4 m depth are not noticeably skewed toward the high-frequency angles. This asymmetry in central-angle displacement suggests that transfers of energy to lower frequencies may be relatively weaker than to higher frequencies. It may also only reflect differences in the directional distribution of high (broad) and low (narrow) frequencies in 10 m depth. An important implication of these observations is that, except near the low-frequency peak of the spectrum, measured shallow-water directional spectra cannot necessarily be used to estimate deep- or shallower-water directional spectra by way of Snell's law.

10. Conclusions

Comparisons between observations of shoaling ocean waves in depths from 4 to 1 m and linear finite-depth theory ((3.1)–(3.3)) indicate that the evolution of many wave-field statistics are not well predicted by linear theory. For example, LFDT does not predict aspects of the power-spectral evolution observed in the field, such as the growth of harmonics of the spectral peak. Improved spectral predictions (figures 2–5) are obtained with the nonlinear Boussinesq model (4.2). For low-energy-wave conditions, the coherence between sensor pairs and component phase velocities of the field data are relatively well predicted by directional LFDT (figure 6). Frequency dispersion is clearly seen at the deepest sensor locations (figure 6*a*). In very shallow water directional LFDT and the normally incident nonlinear model both predict coherences remarkably similar to the data (figure 6*c*). The meaning, if any, of this apparent coincidence is unknown. For higher-energy-wave conditions, the nonlinear model predicts the coherence and phase speed between sensors more accurately than LFDT does, particularly in very shallow water (figures 7 and 8). The effect of phase-locked reflected waves on coherence and phase speed is shown to be not insignificant even for low values of the reflection coefficient (figure 9). Reflected energy is important for frequencies below the spectral peak in the present experiments, and may explain apparent low-frequency phase-speed anomalies observed near coasts and in laboratory basins. Various other wave statistics are also more accurately predicted by the nonlinear model than by LFDT. For example, observed evolution of sea-surface-elevation skewness is qualitatively predicted by the nonlinear model (figure 10), while LFDT has zero skewness. Mean lengths of runs of high waves also show evolution which is better accounted for by the nonlinear model than by LFDT (figure 11).

Changes in the directional spectra between 9 and 3–4 m depths are consistent with the nonlinear generation of high-frequency waves which are directionally aligned with the more energetic low-frequency waves. Thus, the directional distribution of high-frequency waves in very shallow water can be influenced strongly by nonlinearities.

A two-dimensional nonlinear model based on equations such as those given by Peregrine (1967) is needed to model quantitatively this phenomenon. The numerical implementation of such a model for realistic directional spectra is non-trivial.

Support was provided by a grant from the Foundation for Ocean Research (Steve Elgar) and by the Office of Naval Research, Coastal Sciences Branch, under contract number N0014-75-C-0300 (R. T. Guza). The data collection was supported by ONR and the Sea Grant Nearshore Sediment Transport Study (project number RICA-N-40). E. B. Thornton played a central role in all phases of the experiments. R. L. Lowe was the principal engineer. R. J. Seymour obtained the bathymetry and made helpful comments. M. Freilich helped adopt his Boussinesq-equation integration scheme for this application.

REFERENCES

Barber, N. F. 1963 The directional resolving power of an array of wave detectors. In *Ocean Wave Spectra*, pp. 137–150. Prentice-Hall.

Büsching, F. 1978 Anomalous dispersion of Fourier components of surface gravity waves in the nearshore area. In *Proc. 16th Coastal Engineering Conf.*, pp. 247–267. New York: Amer. Soc. Civil Engng.

Elgar, S., Guza, R. T. & Seymour, R. J. 1984 Groups of waves in shallow water. *J. Geophys. Res.* **89**, 3623–3634.

Esteva, D. & Harris, D. L. 1970 Analysis of pressure wave records and surface wave records. In *Proc. 12th Coastal Engng Conf.* pp. 101–116.

Freilich, M. H. & Guza, R. T. 1984 Nonlinear effects on shoaling surface gravity waves. *Phil. Trans. R. Soc. Lond.* A **311**, 1–41.

Gable, C. G. (ed.) 1981 Report on data from the Nearshore Transport Study experiment at Leadbetter Beach, Santa Barbara, California, January–February, 1980. *IMR Ref.* 80-5, Univ. of Calif., Inst. of Marine Resources, La Jolla, CA.

Guza, R. T. & Thornton, E. B. 1980 Local and shoaled comparisons of sea surface elevations, pressures and velocities. *J. Geophys. Res.* **85**, 1524–1530.

Guza, R. T. & Thornton, E. B. 1985*a* Velocity moments in the nearshore. *J. Waterway, Port, Coastal & Ocean Engng* **111**, 235–256.

Guza, R. T. & Thornton, E. B. 1985*b* Observations of surf beat. *J. Geophys. Res.* **90**, 3161–3172.

Holman, R. A. 1981 Infragravity energy in the surf zone. *J. Geophys. Res.* **86**, 6442–6450.

Huang, N. E. 1981 Comment on 'Modulation characteristics of sea surface waves' by A. Ramamonjiarisoa and E. Mollo-Christensen. *J. Geophys. Res.* **86**, 2073–2075.

Huang, N. E. & Tung, C. C. 1977 The influence of the directional energy distribution on the nonlinear dispersion relation in a random gravity wave field. *J. Phys. Oceanogr.* **7**, 403–414.

Inman, D. L., Tait, R. J. & Nordstrom, C. E. 1971 Mixing in the surf zone. *J. Geophys. Res.* **76**, 3493–3514.

Le Méhauté, B. & Wang, J. D. 1982 Wave spectrum changes on a sloped beach. *J. Waterway, Port, Ocean and Coastal Div., Amer. Soc. Civil Eng.* **108**, 33–47.

Munk, W. H., Miller, G. R., Snodgrass, F. E. & Barber, N. F. 1963 Directional recording of swell from distant storms. *Phil. Trans. R. Soc. Lond.* A **255**, 505–584.

Munk, W. H., Snodgrass, F. E. & Gilbert, F. 1964 Long waves on the continental shelf: an experiment to separate trapped and leaky modes. *J. Fluid Mech.* **20**, 529–554.

Oltman-Shay, J. & Guza, R. T. 1985 A data adaptive ocean wave directional spectrum estimator for pitch and roll type measurements. *J. Phys. Oceanogr.* **14**, 1800–1810.

Peregrine, D. H. 1967 Long waves on a beach. *J. Fluid Mech.* **27**, 815–827.

Ramamonjiarisoa, A. & Coantic, M. 1976 Loi expérimentale de dispersion des vagues produits par le vent sur une faible longueur d'action. *C. R. Acad. Sci. Paris* B **282**, 111–113.

Snodgrass, F. E., Groves, G. W., Hasselmann, K. F., Miller, G. R., Munk, W. H. &

POWERS, W. H. 1966 Propagation of ocean swell across the Pacific. *Phil. Trans. R. Soc. Lond.* A **259**, 431–497.

SUHAYDA, J. S. 1974 Standing waves on beaches. *J. Geophys. Res.* **79**, 3065–3071.

THORNTON, E. B. & GUZA, R. T. 1982 Energy saturation and phase speeds measured on a natural beach. *J. Geophys. Res.* **87**, 9499–9508.

YEFIMOV, V. V., SOLOV'YEV, Y. P. & KHRISTOFOROV, G. N. 1972 Observational determination of the phase velocities of spectral components of wind waves. *Isv. Atmos. Oceanic Phys.* **8**, 435–446.